*J Mater Sci* (2023) 58:268–280

Computation & theory

# Monolayer and bilayer lanthanide compound $Gd_2C$ with large magnetic anisotropy energy and high Curie temperature

Yuwan Wang[1], Mohan Yang[2], Zichun Cui[1], Hanghang Zeng[1], Xian Zhang[1], Junqin Shi[1], Tengfei Cao[1], and Xiaoli Fan[1,*]

[1] *State Key Laboratory of Solidification Processing, Center for Advanced Lubrication and Seal Materials, School of Material Science and Engineering, Northwestern Polytechnical University, 127 YouYi Western Road, Xi'an 710072, Shaanxi, China*

[2] *Queen Mary University of London Engineering School, Northwestern Polytechnical University, 127 YouYi Western Road, Xi'an 710072, Shaanxi, China*

**Received:** 9 June 2022
**Accepted:** 25 November 2022
**Published online:**
1 January 2023



## ABSTRACT

Comparing with transition metal compounds, lanthanide compounds hold promising potential as spintronic materials to generate large magnetic moments and strong magnetic anisotropic. By conducting in-depth theoretical calculations, we explored the electronic and magnetic properties of monolayer and bilayer $Gd_2C$, the f-electron lanthanide compound. Monolayer $Gd_2C$ is a ferromagnetic (FM) half-metal with large band gap (1.68 eV) in the semiconducting spin-channel. It has large magnetic anisotropic energy (MAE) (703 μeV/Gd atom), and Curie temperature ($T_C$) of 322 K, above room temperature and higher compared with Gd metal and layered $Gd_2C$. Under 5% biaxial strain, its $T_C$ increases to 392 K. The robust half-metallicity of monolayer $Gd_2C$ is highly desirable for spin current generation and injection. In addition, we found that bilayer $Gd_2C$ maintains to be FM at all stacking orders. Two stable stacking configurations of bilayer $Gd_2C$ were identified; both are FM metals and may coexist at room temperature. Our results demonstrate potential applications of 2D lanthanide compound $Gd_2C$ in the field of spintronics.

## Introduction

2D materials have developed rapidly since the discovery of graphene [1–5]. Nevertheless, 2D materials hardly have intrinsic ferromagnetism [6] according to the Mermin–Wagner theory [7]. Fortunately, large magnetic anisotropic energy (MAE) may offset the thermal fluctuations and maintain long-range magnetic ordering. In addition, the achievement and maintaining of FM order at room temperature and generation of high spin current are crucial for

Handling Editor: Dale Huber.

Address correspondence to E-mail: xlfan@nwpu.edu.cn



https://doi.org/10.1007/s10853-022-08024-8

spintronic devices [8]. Particularly, intrinsic 2D FM semiconductors and half-metals with high $T_C$, large MAE hold promising application prospect in spintronics and the related applications [8–13].

Recently, FM order and semiconducting feature were observed in monolayers $CrX_3$ (X = Cl, Br, I) and bilayer $Cr_2Ge_2Te_6$, but they all exhibited rather low $T_C$ (17 K for $CrCl_3$ [14, 15]; 34 K for $CrBr_3$ [16]; 45 K for $CrI_3$ [17]; and 30 K for $Cr_2Ge_2Te_6$ [18]). Meanwhile, computational studies have predicted various FM semiconducting monolayers, such as $Cr_2I_3X_3$ (X = Cl, Br) ($T_C$ = 26 and 33 K [19]); $MnX_2$ (X = S, Se) ($T_C$ = 225 and 250 K [20]); $CrXTe_3$ (X = Si, Ge) ($T_C$ = 35.7 and 57.2 K [21]); CrOX (X = F, Cl, Br) ($T_C$ = 150, 160 and 129 K [22, 23]). Due to the incompatibility between ferromagnetism and semiconducting [10], the $T_C$ of 2D FM semiconductors is generally below room temperature except for the recent prediction on 1 T′-$CrS_2$ ($T_C$ = 1000 K [24]). FM half-metals may possess higher $T_C$ than FM semiconductors due to the carrier-driven strong exchange interaction [25, 26]. FM half-metallic monolayers, such as $Co_2Se_3$ ($T_C$ = 600 K [27]) and MnX (X = P, As) ($T_C$ = 495 and 711 K [28]) with high $T_C$, have been predicted. It is worth noting that half-metals can provide 100% spin-polarized current and are desirable candidates as pure spin injection [29] and spin transport materials [30].

The intensive investigations on 2D ferromagnets have been focused on transition metal compounds. Nevertheless, lanthanide elements having strong spin–orbit coupling and highly localized 4f electrons [31], offer more potential to generate larger magnetic moments and larger MAE. It is inspiring that 2D FM $GdSi_2$ and $EuSi_2$ were successfully exfoliated from their AFM layered bulks [32]; layered $EuGe_2$ and $GdGe_2$ were synthesized and evolve from typical 3D AFM to 2D FM as their thickness is reduced to few atomic layers [31]. Meanwhile, it has been predicted that monolayer $GdI_2$ has a large magnetic moment (8 $\mu_B$/f.u.) [33]; monolayer $Gd_2B_2$ is a FM metal with a large magnetic moment (7.30 $\mu_B$/Gd) and high $T_C$ up to 550 K [34]. These findings inject new vitality into the applications of lanthanide compounds.

Among the lanthanide elements, Gd is the most noteworthy one. It is the only lanthanide metal with room temperature ferromagnetism [33]. The $T_C$ of Gd metal and its compound $Gd_5Si_4$ is 293 K [35] and 336 K [36], respectively. The layered $Gd_2C$, 2D ferromagnet with $T_C$ of 350 K, was experimentally prepared [37]. Additionally, the electronic property of few-layer $Gd_2C$ was recently studied via first-principles calculations as electrode [38, 39]. The emergence of Weyl semimetal (WSM) phase was discovered in the layered FM $Gd_2C$. The WSM phase of time-reversal symmetry breaking is driven by the combined effects of crystal field, ferromagnetism and spin-orbital coupling (SOC) [39]. Remarkably, 2D layered materials can be stacked in different orders owing to the weak interlayer interaction [40], leading to various properties [41]. The influence of stacking order is particularly outstanding in 2D magnetic materials [12, 17, 18, 42]. Not only varying magnetic orders and electronic properties [17, 18, 43], even new physical phenomena may be obtained via adjusting the stacking order [12, 42].

Motived by the promising potential of lanthanide compounds as spintronic materials, we explored the electronic structure and magnetic coupling of both monolayer and bilayer $Gd_2C$. Via performing the theoretical investigations based on the first-principles methods, we demonstrate the robust ferromagnetism of monolayer $Gd_2C$. It is worth noting that monolayer $Gd_2C$ is an FM half-metal with a large energy gap in the semiconducting spin-channel and a high $T_C$. Under 5% biaxial strain, its $T_C$ increases to 392 K. In addition, we also studied the possible stacking configurations and interlayer magnetic coupling in bilayer $Gd_2C$. It turns out that bilayer $Gd_2C$ has two stable stacking configurations, AB- and AA-stacking; both of them are FM metals with high $T_C$.

## Computational methods

All calculations were performed based on the spin-polarized density function theory (DFT) implemented in the Vienna *ab-initio* calculation package (VASP) [44]. The Perdew–Burke–Ernzerhof (PBE) functional of generalized gradient approximation (GGA) [45] was chosen to describe the exchange correlation interaction. A vacuum space of 15 Å was used to eliminate the interaction between adjacent layers in periodic model [46]. The plane wave cutoff energy was set as 500 eV. All the structures were fully optimized; the convergence criteria for energy and force were set to $10^{-6}$ eV and 0.01 eV/Å, respectively. The gamma-centered 16 × 16 × 1 and 8 × 8 × 1 k-point grids based on the Monkhorst–Pack method [46] were adopt for unit cell and

$2 \times 2 \times 1$ supercell of monolayer and bilayer $Gd_2C$, respectively. The damped van der Waals correction (DFT-D2) method was used to correct the weak interlayer interaction for bilayer $Gd_2C$. Considering the strong correlation interaction of the Gd-4f orbital, we adopted the PBE + U method and set the parameters as U = 9.2 eV and J = 1.2 eV, which has been proved to be reasonable in the previous works [47, 48]. The phonon dispersion calculation was performed on $2 \times 2 \times 1$ supercell using PHONOPY code based on finite-displacement method [49]. For the *ab-initio* molecular dynamics (AIMD) simulation, the NVT ensemble with the Nosé-Hoover thermal bath method was employed to control the temperature [50].

## Results and discussion

### Structure and stability of monolayer $Gd_2C$

Monolayer $Gd_2C$ consists of triple atomic layers forming the sandwich structure where magnetic Gd atoms form two atomic layers of honeycomb lattice. The atomic structure of monolayer $Gd_2C$ that belongs to the $D_{3d}$ point group is depicted in Fig. 1a and e. From Table 1, we can see that the in-plane lattice constant of monolayer $Gd_2C$ is a = b = 3.623 Å, agreeing well with the experimental result of the layered bulk $Gd_2C$ (3.639 Å) [37, 51]. To discern the magnetic ground state of monolayer $Gd_2C$, we calculated the FM configuration and three typical AFM configurations of the hexagonal lattice by using a $2 \times 2 \times 1$ supercell, AFM-zigzag, AFM-stripe and AFM-Néel [52]. The energy differences between FM and AFM configurations shown in Figure S1 indicate that monolayer $Gd_2C$ has a FM ground state. Its magnetic moment is $\sim 8\ \mu_B$ per Gd atom, implying large information storage density. The spin-resolved charge density shows that its magnetic moment mainly attributes to the Gd atoms; the contribution of C atoms is negligible.

To explore the structural stability of monolayer $Gd_2C$, we calculated the cohesive energy as $E_{coh} = (E_{Gd_2C} - 2E_{Gd} - E_C)/3$, where $E_{Gd_2C}$ is the total energy of $Gd_2C$; $E_{Gd}$ and $E_C$ are the energy of isolated Gd and C atoms, respectively. The calculated cohesive energy of monolayer $Gd_2C$ is $-5.94$ eV/atom, suggesting that the Gd–C bonding is quite strong. In addition, the elastic stiffness tensors are calculated to be $C_{11} = 76.46$ N/m ($C_{11} = C_{22}$), $C_{12} = 23.87$ N/m and $C_{66} = 26.29$ N/m, satisfying the Born-Huang criterion ($C_{11} > 0$, $C_{11}C_{22}–C_{12} > 0$ and $C_{66} > 0$) [53] and indicating mechanical stability. The Young's modulus and Poisson's ratio were calculated to be 69.01 N/m and 0.31, via $Y = \left[C_{11}C_{22} - C_{12}^2\right]/C_{11}$ and $v = C_{12}/C_{11}$, respectively. These values are comparable to that of silicene (61 N/m and 0.33) [54] and much lower than that of graphene (342 N/m) [55], suggesting that monolayer $Gd_2C$ is soft and can sustain large strain. As shown in Fig. 2a, there are no imaginary phonon modes, indicating that monolayer $Gd_2C$ is dynamical stable. Furthermore, the thermal stability of the monolayer $Gd_2C$ was assessed by conducting *ab-initio* molecular dynamics (AIMD) [56] simulations at 300 K; the integrity of original configuration and small energy fluctuations confirm its good thermal stability (Fig. 2b).

### Electronic and magnetic properties of monolayer $Gd_2C$

Since PBE-level calculations generally underestimate the band gaps, as shown in Fig. 3a and b, we calculated the electronic structures of the FM monolayer $Gd_2C$ by using the more accurate Heyd–Scuseria–Ernzerhof (HSE06) method [57]. Compared with the results obtained via the PBE + U calculations [38, 39], HSE06 produces similar band structures but with a wider band gap. Notably, the state of the spin-up channel passes through the Fermi level, while the spin-down channel shows semiconducting feature with a band gap of 1.68 eV. Our result indicates that monolayer $Gd_2C$ is an intrinsic FM half-metal. It demonstrates 100% spin polarization at Fermi level, which is highly desirable for pure spin current generation and injection.

The orbital-projected density of states around Femi energy is also plotted in Fig. 3a and b. The states around the Fermi level mainly come from Gd-5d orbitals. The conduction band minimum (CBM) and valence band maximum (VBM) in the semiconducting spin-channel are mainly contributed by Gd atoms. Additionally, there is strong hybridization between Gd-5d and C-2p states at the VBM, implying large exchange interaction between Gd-5d and C-2p electrons. The orbital-projected density of states in the wider energy range (Figure S2) shows that the magnetic moment of monolayer $Gd_2C$ is mainly contributed by the Gd-4f electrons, agreeing well

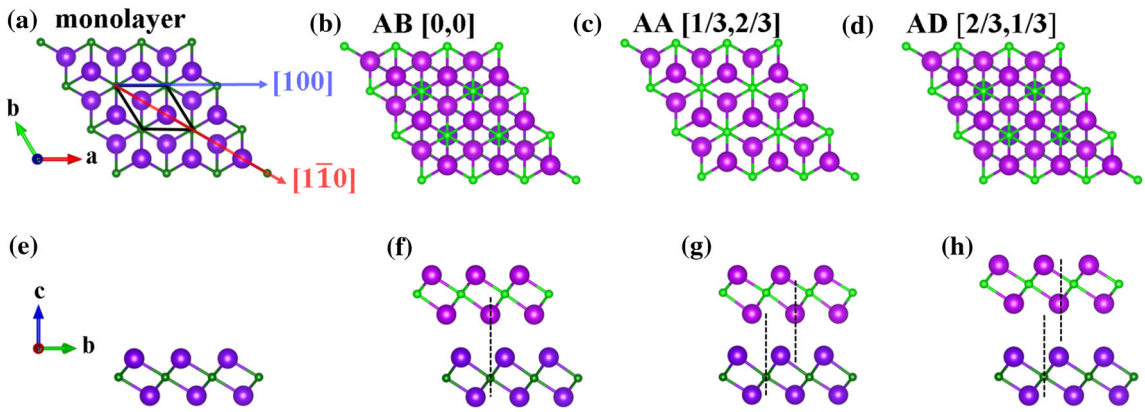


**Figure 1** Top and side views for the atomic structures of monolayer and bilayer $Gd_2C$. (**a**) and (**e**) monolayer $Gd_2C$, (**b**) and (**f**) AB-, (**c**) and (**g**) AA-, (**d**) and (**h**) AD-stacking bilayer $Gd_2C$. The solid parallelogram indicates the unit cell of monolayer $Gd_2C$. The light purple (dark purple) and light green (dark green) balls represent the Gd and C atoms in the top (bottom) layer. The high-symmetrical directions [100] and [1 $\bar{1}$ 0] are marked with blue and red translucent arrows, respectively. In the AB-stacking bilayer $Gd_2C$, the bottom Gd atom in the top $Gd_2C$ layer is directly above the C atom in the bottom $Gd_2C$ layer. The numbers in the square brackets represent the shift of bottom Gd atom in the top layer along the $x$ and $y$ directions relative to the C atom in the bottom $Gd_2C$ layer.

**Table 1** The lattice constant, the bond length between the nearest neighboring (NN) Gd atoms ($d_{Gd-Gd}$), the interlayer distance and the magnetic ground state of bulk, monolayer and bilayer $Gd_2C$

| | Lattice constant (Å) | $d_{Gd-Gd}$(Å) | Interlayer distance | Magnetic ground state |
|---|---|---|---|---|
| Bulk [37, 51] | a = b = 3.639 | 3.46 | 3.38 | FM |
| Monolayer | a = b = 3.623 | 3.42 | | FM |
| AB-stacking | a = b = 3.607 | 3.50 | 3.04 | FM |
| AA-stacking | a = b = 3.609 | 3.51 | 3.01 | FM |

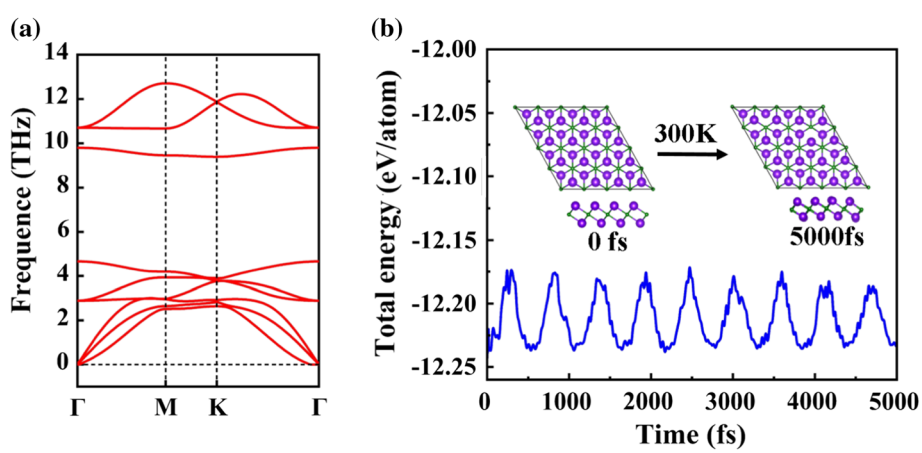


**Figure 2** **a** The phonon dispersion of monolayer $Gd_2C$. **b** Evolution of total energy of monolayer $Gd_2C$ during ab-initio molecular dynamics (AIMD) simulation at 300 K for 5000 fs. The insert diagrams represent the atomic structures of monolayer $Gd_2C$ at the beginning and end of AIMD simulation.

with the results of layered $Gd_2C$ [38]. They are highly localized, showing narrow and high peaks at position far away from the Fermi level.

We considered the intra-atomic and the inter-atomic exchange interactions including the direct-exchange and super-exchange interactions to study the magnetic coupling in monolayer $Gd_2C$. The intra-atomic interaction between Gd-4f and Gd-5d electrons is very strong according to Hund's rule. Consequently, the 5d electrons are spin-polarized near the Fermi level (Fig. 3), and the 4f electrons generate an inherent large magnetic moment through the

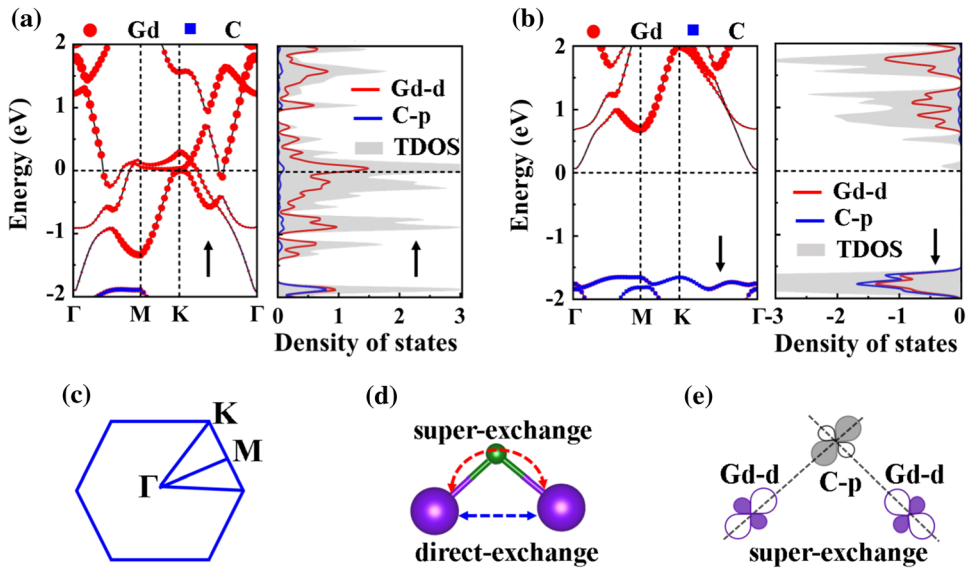


**Figure 3** The band structures and density of states in **a** spin-up and **b** spin-down channels of monolayer $Gd_2C$ calculated by the HSE06 method. The Fermi level ($E_F$) is set to 0 eV. **c** The first Brillouin zone of monolayer $Gd_2C$. Illustration of **d** direct-exchange and **e** super-exchange interactions between Gd atoms.

surrounding polarized 5d electrons [58]. As shown in Fig. 3d and e, the inter-atomic super-exchange interactions between the Gd atoms are mediated through the C atom. According to the Goodenough–Kanamori–Anderson (GKA) rules [59–61], the super-exchange interaction prefers FM coupling because the bond angle of Gd–C–Gd (86.8°) is close to 90°. The considerable hybridization between Gd-5d and C-2p orbitals leads to the strong FM super-exchange interaction. In contrast, the AFM direct-exchange interaction is relatively weak due to the large distance (3.42 Å) between the nearest neighboring (NN) Gd atoms.

Based on Heitler–London model [62], the magnetic exchange parameter J can be represented as $J \approx 2k + 4\beta S$, where $k$ presents the potential exchange; $\beta$ and $S$ are the hopping integral and overlap integral between atomic orbitals. Because the Gd–C–Gd angle is close to 90°, C-2p orbitals are almost orthogonal to Gd-5d orbitals, resulting in S approaching zero. $J$ can be reduced to $2k$, and $k$ is a positive value according to the Hund's rule. Therefore, monolayer $Gd_2C$ prefers FM state and the magnetic coupling is dominated by FM super-exchange interaction.

MAE is defined as the energy difference between the magnetization in the in-plane and out-of-plane directions. Firstly, total energies of monolayer $Gd_2C$ with magnetization directions along the [100], [010] and [001] were calculated to estimate the MAE. Table S1 shows that the MAE along the [100] and [010] directions is 703.5 μeV and 703 μeV per Gd atom, respectively. Our result indicates that the easy magnetization axis of monolayer $Gd_2C$ is along the out-of-plane [001] direction, and the MAE is isotropic along the in-plane directions. Secondly, due to the uniaxial tetragonal symmetry of monolayer $Gd_2C$, the MAE can be described as function of azimuth angle [63]:

$$\mathrm{MAE}(\theta) = K_1 \sin^2\theta + K_2 \sin^4\theta$$

where $K_1$ and $K_2$ are the anisotropy constants, and $\theta$ is the azimuth angle in the $xz$ and $yz$ planes. If $K_1$ is positive and predominates over $K_2$, the magnetization direction is biased to the $z$-axis [001]. Otherwise, the magnetization direction is perpendicular to the $z$-axis. Figure 4a demonstrates the angular dependence of the MAE, which has a good fit with the above equation.

It is sensitive to azimuthal angles, but isotropic in the $xy$ plane. Both $K_1$ and $K_2$ are positive, as listed in table S1. This is similar to monolayers $Fe_3GeTe_2$ [43] and $CrI_3$ [17]. Thirdly, the MAE in the whole space shows strong dependence on the azimuthal angles and isotropic in $xy$ plane. The maximum value of MAE is 703 μeV/Gd atom, which is larger compared with the most known 2D magnetic materials [64, 65]. Such a large perpendicular magnetic anisotropy (PMA) is enough to resist thermal fluctuations and beneficial for higher-density nonvolatile magnetic storage [66, 67].

In order to estimate the $T_C$ of monolayer $Gd_2C$, we performed Monte Carlo (MC) [68] simulation based

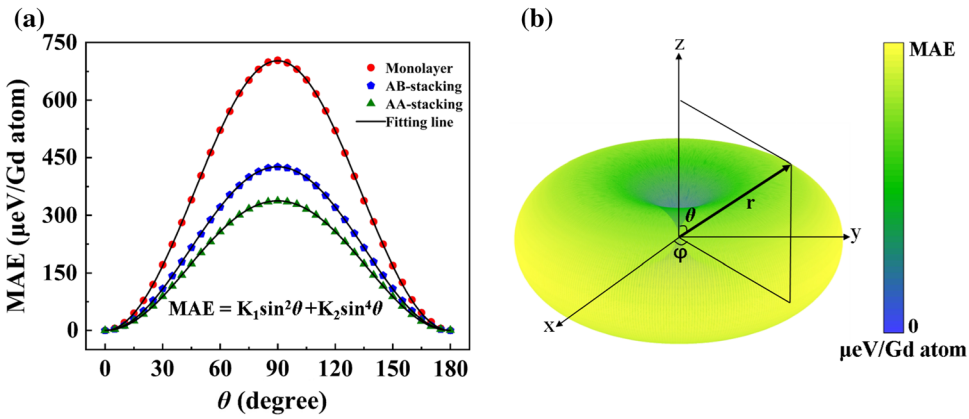


**Figure 4** **a** The magnetic anisotropy energy (MAE) of monolayer $Gd_2C$, AB- and AA-stacking bilayer $Gd_2C$ as a function of the azimuth angle $\theta$. The out-of-plane [001] magnetization energies were taken as a reference. **b** Schematic diagram showing MAE of monolayer $Gd_2C$, AB- and AA-stacking bilayer $Gd_2C$ as function of polar angle and azimuthal angle. The $\varphi$ and $\theta$ are the polar angle in the $xy$ plane, and the azimuthal angle in the $xz$ and $yz$ planes. The color saturation and radical length represent the energy required to rotate the magnetic axis into a certain direction.

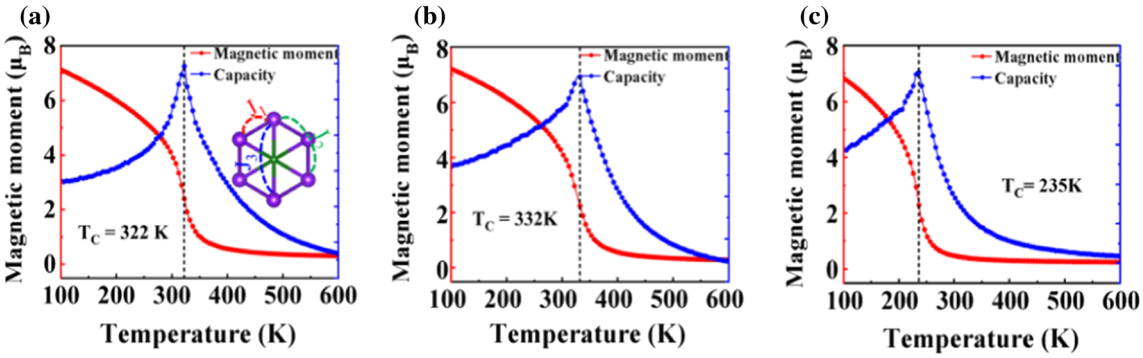


**Figure 5** The variation of magnetic moment of Gd atoms and the specific heat as a function of temperature for **a** monolayer $Gd_2C$, **b** AB- and **c** AA-stacking bilayer $Gd_2C$ based on the Heisenberg model. The inset diagram shows the magnetic exchange interaction between the nearest neighboring (NN) ($J_1$), second NN (2NN) ($J_2$) and third NN (3NN) ($J_3$) Gd atoms.

on the Heisenberg model [69]. The spin Hamiltonian is expressed as:

$$H = -\sum_{ij} J_1 S_i S_j - \sum_{ik} J_2 S_i S_k - \sum_{ih} J_3 S_i S_h - A S_i^Z S_i^Z$$

where $J_1$, $J_2$ and $J_3$ are the magnetic exchange parameters between NN, second NN (2NN) and third (NN) (3NN) Gd atoms (Fig. 5a), respectively. $S_i$ is the spin vector of magnetic atom, $S_i^Z$ is the $Z$ component of the spin vector, and $A$ represents the anisotropy parameter, which was calculated via the MAE. A supercell of $32 \times 32 \times 1$ was used. We considered FM and three AFM configurations, and their total energies are descried as

$$E(\text{FM}) = E_0 - (12J_1 + 24J_2 + 12J_3)|S|^2$$

$$E(\text{AFM-zizag}) = E_0 - (4J_1 - 8J_2 - 12J_3)|S|^2$$

$$E(\text{AFM-stripe}) = E_0 - (-4J_1 - 8J_2 + 12J_3)|S|^2$$

$$E(\text{AFM-Néel}) = E_0 - (-12J_1 + 24J_2 - 12J_3)|S|^2$$

Through the above four equations, the magnetic exchange parameters $J_1$, $J_2$ and $J_3$ are calculated to be 1.07, 0.73 and 0.53 meV, respectively. The positive values indicate the FM coupling between the NN, 2NN and 3NN Gd atoms.

Figure 5a shows the evolutions of magnetic moment of Gd atom and heat capacity ($C_V$) as temperature. The heat capacity is defined as $C_V = \frac{(\langle E^2\rangle - \langle E\rangle^2)}{k_B T^2}$. The $T_C$ was estimated from the

position where the magnetic moment drops sharply and the peak positions of $C_V$. Our calculation shows that the $T_C$ of the monolayer $Gd_2C$ is 322 K, higher than that of Gd metal (293 K) [35], slightly lower than those of compound $Gd_5Si_4$ (336 K) [36] and the layered $Gd_2C$ (350 K) [37]. The above room temperature of $T_C$ and half-metallic behavior of monolayer $Gd_2C$ make it a promising candidate material for spintronic devices.

## The magnetic property of monolayer $Gd_2C$ under biaxial strain

2D materials are usually synthesized on suitable substrates. The lattice mismatch between 2D material and substrate usually causes strain on 2D material and changes its properties [70]. Here we studied monolayer $Gd_2C$ under $-5\% \sim 5\%$ biaxial strain. Figure S3 shows that under strain of $-5\% \sim 5\%$, the CBM of spin-down channel is slightly across the Fermi level around Γ point. Our calculation shows that monolayer $Gd_2C$ under 5% strain still can generate 100% spin-polarized current by applying a small electric field to low down the Fermi level, as shown in Figure S4.

Figure 6a shows the energy difference ($\Delta E = E_{AFM} - E_{FM}$) between the FM and AFM configurations of monolayer $Gd_2C$ under biaxial strain. The ΔE is positive and increases monotonically under the biaxial strain from − 5% to 5%. This indicates that the FM coupling between Gd atoms is weakened and strengthened under the increased compressive and tensile strain, respectively. Figure 6b shows the distance ($d_1$) between the NN Gd atoms is almost constant under $-5\% \sim 5\%$ biaxial strain. The distances between 2NN ($d_2$) and 3NN ($d_3$) Gd atoms decrease monotonically with the increasing compressive strain, making the direct-exchange interactions stronger. The bond angles θ of Gd–C–Gd increase monotonically approaching 90°, leading to enhanced super-exchange interactions. However, the direct- and super-exchange interactions weaken, while $d_2$ and $d_3$ increase and the bond angle θ of Gd–C–Gd decreases away from 90° as the tensile strain is increased. The delicately competing nature of direct- and super-exchange interactions leads to the robust FM coupling of monolayer $Gd_2C$ under $-5\% \sim 5\%$ biaxial strain. We also calculated the MAE. Its value decreases as the biaxial strain is changing from − 5% to 4%. Under 5% tensile strain, the value of MAE changes to be negative, which indicates that the easy magnetization axis converts from the out-of-plane direction to the in-plane direction. Our results

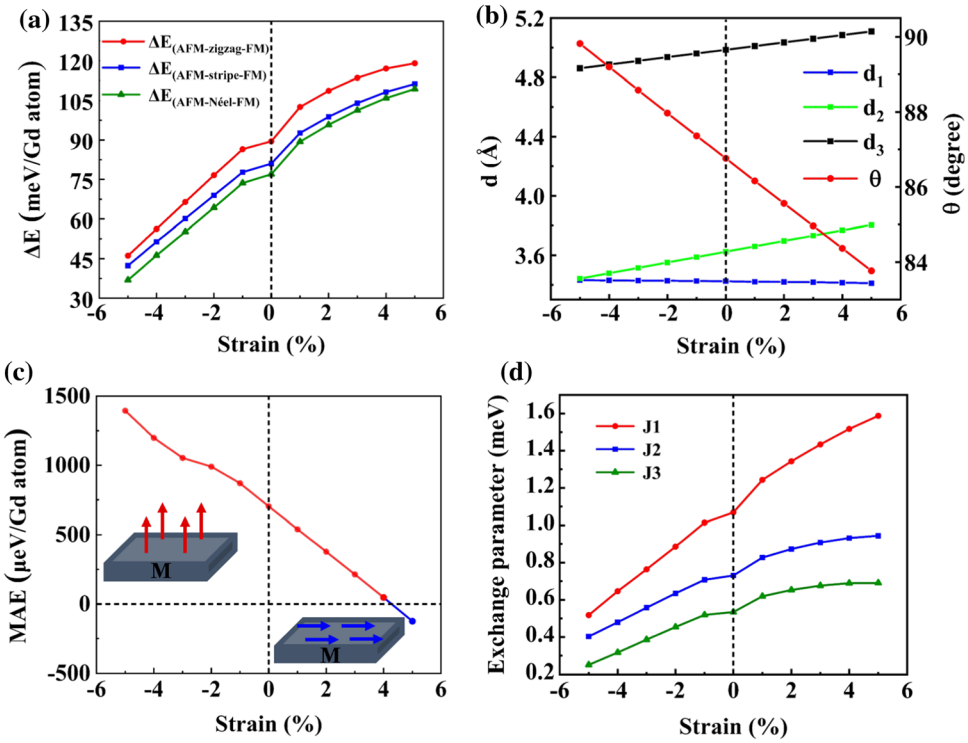


**Figure 6** **a** The energy difference (ΔE) between ferromagnetic (FM) and three antiferromagnetic (AFM) configurations, **b** the distance between the nearest neighboring (NN) ($d_1$), second NN (2NN) ($d_2$) and third NN (3NN) ($d_3$) Gd atoms, and Gd–C–Gd bond angle θ, **c** the magnetic anisotropy energy (MAE) and **d** the exchange parameters of monolayer $Gd_2C$ under biaxial strain of $-5\% \sim 5\%$. MAE greater/less than zero represents the out-of-plane/in-plane magnetization direction.

suggest that strain can be used to tune the magnetization orientation of monolayer $Gd_2C$.

The calculated $J_1$, $J_2$ and $J_3$ of monolayer $Gd_2C$ under $-5\% \sim 5\%$ biaxial strain is shown in Fig. 6d. It indicates that $J_1$, $J_2$ and $J_3$ increase monotonically under the biaxial strain from $-5\%$ to 5%. Correspondingly, Figure S5 shows that the $T_C$ of the monolayer $Gd_2C$ drops to 182 K at the compressive biaxial strain of $-5\%$, but rises to 392 K at the tensile biaxial strain of 5%. This is consistent with the monotonic enhancement of $T_C$ for most systems under tension [20, 21, 71, 72].

## Configurations of bilayer $Gd_2C$

There are three high-symmetrical sites on the surface of monolayer $Gd_2C$: above the C atoms ($M_C$), above bottom Gd atoms ($B_{Gd}$), above the top Gd atoms ($T_{Gd}$). Correspondingly, three configurations of bilayer $Gd_2C$ with the bottom Gd atom in the top $Gd_2C$ layer locating on the three sites are constructed. As shown in Fig. 1, the three configurations of bilayer $Gd_2C$ are named as AB-, AA- and AD-stacking. Notably, AB-stacking is indeed the stacking configuration of the layered bulk $Gd_2C$. Our calculations show that the interlayer distances of the AB-, AA- and AD-stackings bilayer $Gd_2C$ are 3.04, 3.01 and 3.51 Å, respectively. AB-stacking is energetically most favorable; the energies of AA- and AD-stackings are 1.6 and 147.9 meV/Gd atom higher than that of AB-stacking, respectively. The results show that the interlayer distance and the interlayer stacking energy of bilayer $Gd_2C$ are sensitive to the stacking configuration.

Various stacking configurations may be obtained via physical, structural and chemical approaches [73], which provides a possible way to adjust the electronic and magnetic properties of bilayer $Gd_2C$. In this context, by rigidly and laterally sliding the top $Gd_2C$ layer along the high symmetry directions [100] and [1 $\bar{1}$ 0], we explored the other possible stacking configurations of bilayer $Gd_2C$. The interlayer stacking energy and the interlayer exchange energy were calculated for each stacking configuration, and the results are shown in Fig. 7a and b. AB-stacking has the lowest energy; the energy of the AA-stacking is slightly higher than that of the AB-stacking; AD-stacking has the highest energy. Except for the AA- and AB-stacking, no other energetically stable stacking configuration was identified.

As shown in Fig. 7b, all stacking configurations generated via top $Gd_2C$ layer sliding along the two symmetrical routes [100] and [1 $\bar{1}$ 0] maintain the FM interlayer coupling. More stackings via sliding the top $Gd_2C$ layer along the entire $xy$ plane were studied. As shown in Fig. 7c and d, AB-stacking still has the lowest energy; all the investigated stacking configurations energetically prefer the FM interlayer coupling. In addition, the stacking-constraint relaxations in the $z$-direction were performed as stacking affects the interlayer distance. As shown in Figure S6 (a) and (b), both the interlayer stacking energy and the interlayer exchange energy change with maintaining the overall trends. The AB-stacking bilayer $Gd_2C$ is still the global minimum, and the energy of AA-stacking is 1.6 meV/Gd atom higher than that of AB-stacking. The stacking order does not change the ferromagnetism of bilayer $Gd_2C$.

Adopting the CI-NEB method [74], we further calculated the minimum energy path for the stacking transition reaction of bilayer $Gd_2C$ from AB- to AA-stacking. As shown in Figure S7, there is an energy barrier of about 200 meV/unit cell, which will prevent the transition from AB- to AA-stacking at room temperature [75]. Our calculations predict two stable stacking configurations for bilayer $Gd_2C$ which may co-exist at room temperature.

## Electronic and magnetic properties of AB- and AA-stacking bilayer $Gd_2C$

Using the HSE06 function the spin-resolved band structures of AB- and AA-stacking bilayer $Gd_2C$ were calculated and are shown in Fig. 8a and b. Unlike the half-metallic monolayer $Gd_2C$, both AB- and AA-stacking bilayer $Gd_2C$ exhibit metallic behavior. As shown in the schematic diagram, both the spin-up and the spin-down channels pass through the Fermi level. As shown in Figure S8 (a) and (b) for the orbital-projected density of states, Gd-4f electrons of the AB- and AA-stacking bilayer $Gd_2C$ are highly localized and spin-polarized. They are the major contributor to the magnetic moment but do not participate in the intralayer or interlayer exchange interaction.

As listed in Table S1, the energies of the AB- and AA-stacking bilayer $Gd_2C$ with magnetization direction along the [001] are lower than that along the [100] and [010] directions, and the energies along the [100] and [010] directions are almost same. Our

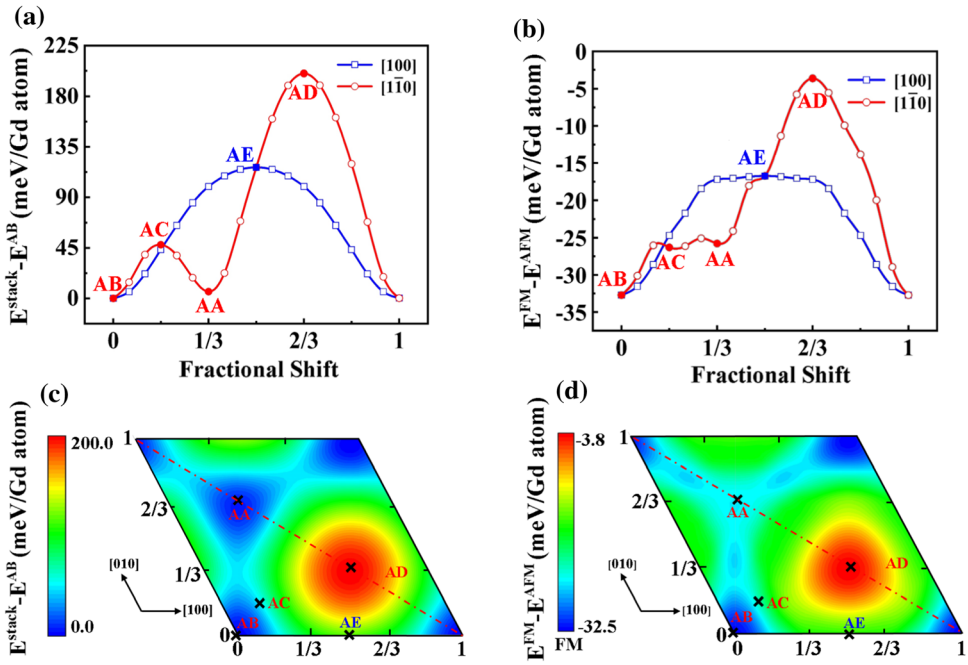


**Figure 7** The evolution of the interlayer stacking energy and exchange energy of bilayer $Gd_2C$ with respect to the rigidly and laterally sliding of one $Gd_2C$ layer along the high-symmetrical [100] (solid blue line) and [1 $\bar{1}$ 0] (solid red line) directions (**a**) and (**b**), and the *xy* plane (**c**) and (**d**). In the AB-stacking bilayer $Gd_2C$, the bottom Gd atom in the top $Gd_2C$ layer is directly above the C atom in the bottom $Gd_2C$ layer. In the AC-, AA-, AD- and AE-stacking bilayer $Gd_2C$, the bottom Gd atom in the top $Gd_2C$ layer is displaced by [1/6, − 1/6], [1/3, 2/3], [2/3, 1/3] and [1/2, 0] relative to the C atom in the bottom $Gd_2C$ layer.

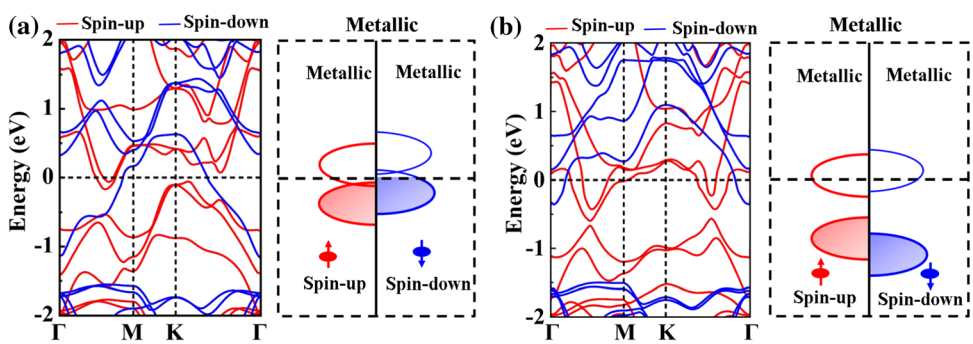


**Figure 8** The spin-resolved band structures calculated by the HSE06 method and the schematic diagram showing the spin-resolved density of states for **a** AB- and **b** AA-stacking bilayer $Gd_2C$. The Fermi level ($E_F$) is set to 0 eV.

results indicate that the easy magnetization axis of AB- and AA-stacking bilayer $Gd_2C$ is along the out-of-plane [001] direction. The angle dependence of MAE is shown in Fig. 4a and b. Consistent with monolayer $Gd_2C$, the MAE of the two stacking configurations of bilayer $Gd_2C$ is all sensitive to the azimuthal angle on *xz* and *yz* planes but is independent of the polar angle on *xy* plane. The maximum MAE is 427 and 338 μeV/Gd atom for AB- and AA-stacking bilayer $Gd_2C$, respectively.

The magnetic coupling in AB- and AA-stacking bilayer $Gd_2C$ was investigated by using the equation $H = -\sum_{ij} J_{\text{intra}} S_i S_j - \sum_{ij} J_{\text{inter}} S_i S_k$. $J_{\text{intra}}$ represents the intralayer exchange interaction, including the exchange interactions between intralayer NN ($J_{11}$), 2NN ($J_{22}$) and 3NN ($J_{33}$) Gd atoms. $J_{\text{inter}}$ represents the interlayer exchange interaction of NN Gd atoms. The possible magnetic configuration of bilayer $Gd_2C$ is shown in Figure S9. The energy of AB-stacking bilayer $Gd_2C$ can be expressed as:

$$E_{\text{FM}}^{\text{FM}} = E_0 - (24J_{11} + 48J_{22} + 24J_{33})|S|^2 - 12J_{\text{inter}}|S|^2$$

$$E_{\text{FM}}^{\text{AFM}} = E_0 - (24J_{11} + 48J_{22} + 24J_{33})|S|^2 + 12J_{\text{inter}}|S|^2$$

$$E_{\text{AFM-zigzag}}^{\text{FM}} = E_0 - (8J_{11} - 16J_{22} - 24J_{33})|S|^2 + 4J_{\text{inter}}|S|^2$$

$$E^{\mathrm{AFM}}_{\mathrm{AFM-stripe}} = E_0 - (-8J_{11} - 16J_{22} + 24J_{33})|S|^2 - 4J_{\mathrm{inter}}|S|^2$$

$$E^{\mathrm{AFM}}_{\mathrm{AFM-Neel}} = E_0 - (-24J_{11} + 48J_{22} - 24J_{33})|S|^2 + 12J_{\mathrm{inter}}|S|^2$$

The superscript and subscript indicate the interlayer and intralayer magnetic coupling, respectively. The calculated exchange parameters $J_{11}$, $J_{22}$, $J_{33}$ and $J_{\mathrm{inter}}$ for the AB-/AA-stacking bilayer $Gd_2C$ are 0.64/0.45, 0.59/0.44, 0.22/0.17 and 1.22/0.82 meV, respectively. We find that both the intralayer and interlayer magnetic coupling for AB- and AA-stacking bilayer $Gd_2C$ are FM. The interlayer exchange interaction of AB- and AA-stackings bilayer $Gd_2C$ is at the same level as those of $Cr_2Ge_2Te_6$ [18] and $RuCl_3$ [76] and is dominant over the intralayer interaction. Compared with monolayer $Gd_2C$, the intralayer exchange interactions in AB- and AA-stacking bilayer $Gd_2C$ are significantly lower.

Differential charge density (DCD) of AB- and AA-stacking bilayer $Gd_2C$ is shown in Figure S10. Comparing with $CrS_2$ [77], the interlayer electronic hybridization of bilayer $Gd_2C$ is quite strong. Specifically, there is significant charge reduction near the bottom Gd atom of the top $Gd_2C$ layer and the top Gd atom of the bottom $Gd_2C$ layer. Charge accumulation occurs in the middle region between top and bottom $Gd_2C$ layers. The bottom Gd atom in the top $Gd_2C$ layer and the top Gd atom in the bottom $Gd_2C$ layer share considerable electrons, weakening intralayer Gd–C bonding and reducing intralayer exchange interaction.

Based on the calculated magnetic coupling parameters and the Heisenberg model, we calculated the $T_C$ of AB- and AA-stacking bilayer $Gd_2C$. As shown in Fig. 5b and c, the $T_C$ of AB-stacking bilayer $Gd_2C$ is 332 K, higher than room temperature and slightly higher than that of monolayer $Gd_2C$. The $T_C$ of the AA-stacking bilayer $Gd_2C$ is 235 K, lower than that of the monolayer $Gd_2C$. Consistently, the intralayer and interlayer exchange constants of AB-stacking are greater than those of AA-stacking. The $T_C$ of the AA-stacking bilayer $Gd_2C$ is 235 K, lower than that of the monolayer $Gd_2C$.

## Conclusions

In summary, our results demonstrate that monolayer $Gd_2C$ is an FM half-metal, having good stability and large magnetic moment ($\sim$ 8 $\mu_B$/Gd) along the out-of-plane direction. Plus, monolayer $Gd_2C$ has a large MAE and its $T_C$ is predicted to be above room temperature (322 K). Under small biaxial strain ($-$ 5% $\sim$ 5%), monolayer $Gd_2C$ maintains to be FM and could generate 100% spin-polarized current via applying a small electric field. Its $T_C$ rises to 392 K, and its magnetization direction changes from the out-of-plane direction to the in-plane direction under 5% tensile biaxial strain. We found that bilayer $Gd_2C$ prefers FM interlayer coupling, and identified two stable stacking configurations. The two staking configurations may co-exist at room temperature, and their $T_C$ is predicted to be 332 K and 235 K based on the Heisenberg model, respectively. We propose a new stable FM monolayer and bilayer lanthanide compound $Gd_2C$ with large magnetic moment and high $T_C$. The robust FM half-metallicity of monolayer $Gd_2C$ is highly desired to the applications in the field of spintronics.

## Acknowledgements

This work was supported by the Natural Science Fund of Shaanxi Province for distinguished Young Scholars (2019JC-10) and key project (2021JZ-07), the Polymer Electromagnetic Functional Materials Innovation Team of Shaanxi Sanqin Scholars.

## Declarations

**Conflict of interest** The authors declare no competing financial or personal interests that could have influenced the work reported in this article.

**Supplementary Information:** The online version contains supplementary material available at https://doi.org/10.1007/s10853-022-08024-8.

## References

[1] Novoselov KS, Geim AK, Morozov SV, Jiang D, Zhang Y, Dubonos SV, Grigorieva IV, Firsov AA (2004) Electric field effect in atomically thin carbon films. Science 306:666–669

[2] Li H, Zhang Q, Yap CCR, Tay BK, Edwin THT, Olivier A, Baillargeat D (2012) From bulk to monolayer $MoS_2$: evolution of Raman scattering. Adv Funct Mater 22:1385–1390
[3] Bonaccorso F, Colombo L, Yu G, Stoller M, Tozzini V, Ferrari AC, Ruoff RS, Pellegrini V (2015) Graphene, related two-dimensional crystals, and hybrid systems for energy conversion and storage. Science 347:1246501
[4] Li X, Yin J, Zhou J, Guo W (2014) Large area hexagonal boron nitride monolayer as efficient atomically thick insulating coating against friction and oxidation. Nanotechnology 25:105701
[5] Tan C, Cao X, Wu X-J, He Q, Yang J, Zhang X, Chen J, Zhao W, Han S, Nam G-H, Sindoro M, Zhang H (2017) Recent advances in ultrathin two-dimensional nanomaterials. Chem Rev 117:6225–6331
[6] Wang Y, Anh P, Li S, Yi J (2016) Electronic and magnetic properties of transition-metal-doped monolayer black phosphorus by defect engineering. J Phys Chem C 120:9773–9779
[7] Mermin ND, Wagner H (1966) Absence of ferromagnetism or antiferromagnetism in one-or two-dimensional isotropic Heisenberg models. Phys Rev Lett 17:1133–1136
[8] Li X, Yang J (2016) First-principles design of spintronics materials. Natl Sci Rev 3:365–381
[9] Zhang S, Xu R, Duan W, Zou X (2019) Intrinsic half-metallicity in 2D ternary chalcogenides with high critical temperature and controllable magnetization direction. Adv Funct Mater 29:1808380
[10] Feng YP, Shen L, Yang M, Wang A, Zeng M, Wu Q, Chintalapati S, Chang C-R (2017) Prospects of spintronics based on 2D materials. Wiley Interdiscip Rev Comput Mol Sci 7:e1313
[11] Li H, Ruan S, Zeng Y-J (2019) Intrinsic van der Waals magnetic materials from bulk to the 2D limit: new frontiers of spintronics. Adv Mater 31:1900065
[12] Gibertini M, Koperski M, Morpurgo AF, Novoselov KS (2019) Magnetic 2D materials and heterostructures. Nat Nanotechnol 14:408–419
[13] Sethulakshmi N, Mishra A, Ajayan PM, Kawazoe Y, Roy AK, Singh AK, Tiwary CS (2019) Magnetism in two-dimensional materials beyond graphene. Mater Today 27:107–122
[14] Cai X, Song T, Wilson NP, Clark G, He M, Zhang X, Taniguchi T, Watanabe K, Yao W, Xiao D, McGuire MA, Cobden DH, Xu X (2019) Atomically thin $CrCl_3$: an in-plane layered antiferromagnetic insulator. Nano Lett 19:3993–3998
[15] McGuire MA, Clark G, Santosh KC, Chance WM, Jellison GE Jr, Cooper VR, Xu X, Sales BC (2017) Magnetic behavior and spin-lattice coupling in cleavable van der Waals layered $CrCl_3$ crystals. Phys Rev Mater 1:014001
[16] Zhang Z, Shang J, Jiang C, Rasmita A, Gao W, Yu T (2019) Direct photoluminescence probing of ferromagnetism in monolayer two-dimensional $CrBr_3$. Nano Lett 19:3138–3142
[17] Huang B, Clark G, Navarro-Moratalla E, Klein DR, Cheng R, Seyler KL, Zhong D, Schmidgall E, McGuire MA, Cobden DH, Yao W, Xiao D, Jarillo-Herrero P, Xu X (2017) Layer-dependent ferromagnetism in a van der Waals crystal down to the monolayer limit. Nature 546:270–273
[18] Gong C, Li L, Li Z, Ji H, Stern A, Xia Y, Cao T, Bao W, Wang C, Wang Y, Qiu ZQ, Cava RJ, Louie SG, Xia J, Zhang X (2017) Discovery of intrinsic ferromagnetism in two-dimensional van der Waals crystals. Nature 546:265–269
[19] Zhang F, Mi W, Wang X (2019) Spin-dependent electronic structure and magnetic anisotropy of 2D ferromagnetic Janus $Cr_2I_3X_3$ (X = Br, Cl) monolayers. Adv Electron Mater 6:1900778
[20] Kan M, Adhikari S, Sun Q (2014) Ferromagnetism in $MnX_2$ (X = S, Se) monolayers. Phys Chem Chem Phys 16:4990–4994
[21] Li X, Yang J (2014) $CrXTe_3$ (X = Si, Ge) nanosheets: two dimensional intrinsic ferromagnetic semiconductors. J Mater Chem C 2:7071–7076
[22] Miao N, Xu B, Zhu L, Zhou J, Sun Z (2018) 2D intrinsic ferromagnets from van der Waals antiferromagnets. J Am Chem Soc 140:2417–2420
[23] Xiao T, Wang G, Liao Y (2018) Theoretical prediction of two-dimensional CrOF sheet as a ferromagnetic semiconductor or a half-metal. Chem Phys 513:182–187
[24] Chen K, Deng J, Yan Y, Shi Q, Chang T, Ding X, Sun J, Yang S, Liu JZ (2021) Diverse electronic and magnetic properties of $CrS_2$ enabling strain-controlled 2D lateral heterostructure spintronic devices, npj Comput. Mater 7:79
[25] Zener C (1951) Interaction between the d-Shells in the transition metals. II. Ferromagnetic compounds of manganese with Perovskite structure. Phys Rev 82:403–405
[26] Huang C, Feng J, Wu F, Ahmed D, Huang B, Xiang H, Deng K, Kan E (2018) Toward intrinsic room-temperature ferromagnetism in two-dimensional semiconductors. J Am Chem Soc 140:11519–11525
[27] Lv P, Tang G, Yang C, Deng J, Liu Y, Wang X, Wang X, Hong J (2018) Half-metallicity in two-dimensional $Co_2Se_3$ monolayer with superior mechanical flexibility. 2D Mater 5:045026
[28] Wang B, Zhang Y, Ma L, Wu Q, Guo Y, Zhang X, Wang J (2019) MnX (X = P, As) monolayers: a new type of two-dimensional intrinsic room temperature ferromagnetic half-metallic material with large magnetic anisotropy. Nanoscale 11:4204–4209

[29] Belashchenko KD, Glasbrenner JK, Wysocki AL (2012) Spin injection from a half-metal at finite temperatures. Phys Rev B 86:224402
[30] Ohnuma Y, Matsuo M, Maekawa S (2016) Spin transport in half-metallic ferromagnets. Phys Rev B 94:184405
[31] Tokmachev AM, Averyanov DV, Taldenkov AN, Parfenov OE, Karateev IA, Sokolov IS, Storchak VG (2019) Lanthanide f(7) metalloxenes - a class of intrinsic 2D ferromagnets. Mater Horiz 6:1488–1496
[32] Tokmachev AM, Averyanov DV, Parfenov OE, Taldenkov AN, Karateev IA, Sokolov IS, Kondratev OA, Storchak VG (2018) Emerging two-dimensional ferromagnetism in silicene materials. Nat Commun 9:1672
[33] Wang B, Zhang X, Zhang Y, Yuan S, Guo Y, Dong S, Wang J (2020) Prediction of a two-dimensional high-T-C f-electron ferromagnetic semiconductor. Mater Horiz 7:1623–1630
[34] Gorkan T, Vatansever E, Akinci U, Gokoglu G, Akturk E, Ciraci S (2020) Above room temperature ferromagnetism in $Gd_2B_2$ monolayer with high magnetic anisotropy. J Phys Chem C 124:12816–12823
[35] Nigh HE, Legvold S, Spedding FH (1963) Magnetization and electrical resistivity of gadolinium single crystals. Phys Rev 132:1092–1097
[36] Holtzberg F, Gambino RJ, McGuire TR (1967) New ferromagnetic 5: 4 compounds in the rare earth silicon and germanium systems. J Phys Chem Solids 28:2283–2289
[37] Lee SY, Hwang JY, Park J, Nandadasa CN, Kim Y, Bang J, Lee K, Lee KH, Zhang Y, Ma Y, Hosono H, Lee YH, Kim SG, Kim SW (2020) Ferromagnetic quasi-atomic electrons in two-dimensional electride. Nat Commun 11:1–8
[38] Liu S, Wang C, Liu L, Choi J-H, Kim H-J, Jia Y, Park CH, Cho J-H (2020) Ferromagnetic weyl fermions in two-dimensional layered electride $Gd_2C$. Phys Rev Lett 125:187203
[39] Chae J, Lee J, Oh Y, Kim G (2021) First-principles study of two-dimensional electron gas on a layered $Gd_2C$ electride surface. Phys Rev B 104:125403
[40] Geim AK, Grigorieva IV (2013) Van der Waals heterostructures. Nature 499:419–425
[41] Zhou Y, Maity N, Rai A, Juneja R, Meng X, Roy A, Zhang Y, Xu X, Lin J-F, Banerjee SK, Singh AK, Wang Y (2020) Stacking-order-driven optical properties and carrier dynamics in $ReS_2$. Adv Mater 32:1908311
[42] Long C, Wang T, Jin H, Wang H, Dai Y (2020) Stacking-independent ferromagnetism in bilayer $VI_3$ with half-metallic characteristic. J Phys Chem Lett 11:2158–2164
[43] Zhuang HL, Kent PRC, Hennig RG (2016) Strong anisotropy and magnetostriction in the two-dimensional Stoner ferromagnet $Fe_3GeTe_2$. Phys Rev B 93:134407
[44] Kresse G, Furthmuller J (1996) Efficient iterative schemes for ab initio total-energy calculations using a plane-wave basis set. Phys Rev B 54:11169–11186
[45] Perdew JP, Burke K, Ernzerhof M (1996) Generalized gradient approximation made simple. Phys Rev Lett 77:3865–3868
[46] Monkhorst HJ, Pack JD (1976) Special points for Brillouin-zone integrations. Phys Rev B 13:5188–5192
[47] Larson P, Lambrecht WRL, Chantis A, van Schilfgaarde M (2007) Electronic structure of rare-earth nitrides using the LSDA plus U approach: importance of allowing 4f orbitals to break the cubic crystal symmetry. Phys Rev B 75:045114
[48] Jamnezhad H, Jafari M (2017) Structural, electronic, and optical properties of C-type $Gd_2O_3$: a density functional theory investigation. J Comput Electron 16:272–279
[49] Baroni S, de Gironcoli S, Dal Corso A, Giannozzi P (2001) Phonons and related crystal properties from density-functional perturbation theory. Rev Mod Phys 73:515–562
[50] Martyna GJ, Klein ML, Tuckerman M (1992) Nosé-Hoover chains: the canonical ensemble via continuous dynamics. J Chem Phys 97:2635–2643
[51] Mudryk Y, Paudyal D, Pecharsky VK, Gschneidner KA Jr (2011) Magnetic properties of $Gd_2C$: experiment and first principles calculations. J Appl Phys 109:07A924
[52] Dong X-J, You J-Y, Gu B, Su G (2019) Strain-induced room-temperature ferromagnetic semiconductors with large anomalous hall conductivity in two-dimensional $Cr_2Ge_2Se_6$. Phys Rev Appl 12:014020
[53] Born M, Huang K, Lax M (1955) Dynamical theory of crystal lattices. Am J Phys 23:274
[54] Zhang H, Wang R (2011) The stability and the nonlinear elasticity of 2D hexagonal structures of Si and Ge from first-principles calculations. Phys B 406:4080–4084
[55] Lee C, Wei X, Kysar JW, Hone J (2008) Measurement of the elastic properties and intrinsic strength of monolayer graphene. Science 321:385–388
[56] Nosé S (1984) A unified formulation of the constant temperature molecular dynamics methods. J Chem Phys 81:511–519
[57] Heyd J, Scuseria GE, Ernzerhof M (2003) Hybrid functionals based on a screened Coulomb potential. J Chem Phys 118:8207–8215
[58] Roy LE (2006) Rules for understanding rare-earth magnetic compounds. Texas A&M University, Texas
[59] Goodenough JB (1955) Theory of the role of covalence in the perovskite-type manganites [La, M(II)]$Mn_O$3. Phys Rev 100:564–573
[60] Kanamori J (1960) Crystal distortion in magnetic compounds. J Appl Phys 31:S14–S23

[61] Anderson PW (1959) New approach to the theory of superexchange interactions. Phys Rev 115:2–13
[62] Launay J-P, Verdaguer M (2013) Electrons in molecules: from basic principles to molecular electronics. Oxford University Press, Oxford
[63] Buschow KHJ, de Boer FR (2003) Physics of magnetism and magnetic materials. Kluwer Academic/Plenum Publishers, New York
[64] Ashton M, Gluhovic D, Sinnott SB, Guo J, Stewart DA, Hennig RG (2017) Two-dimensional intrinsic half-metals with large spin gaps. Nano Lett 17:5251–5257
[65] Zhuang HL, Hennig RG (2016) Stability and magnetism of strongly correlated single-layer $VS_2$. Phys Rev B 93:054429
[66] Ikeda S, Miura K, Yamamoto H, Mizunuma K, Gan HD, Endo M, Kanai S, Hayakawa J, Matsukura F, Ohno H (2010) A perpendicular-anisotropy CoFeB-MgO magnetic tunnel junction. Nat Mater 9:721–724
[67] Bhatti S, Sbiaa R, Hirohata A, Ohno H, Fukami S, Piramanayagam SN (2017) Spintronics based random access memory: a review. Mater Today 20:530–548
[68] Evans RFL, Fan WJ, Chureemart P, Ostler TA, Ellis MOA, Chantrell RW (2014) Atomistic spin model simulations of magnetic nanomaterials. J Phys Condens Matter 26:103202
[69] Webster L, Yan J-A (2018) Strain-tunable magnetic anisotropy in monolayer $CrCl_3$, $CrBr_3$, and $CrI_3$. Phys Rew B 98:144411
[70] Si C, Sun Z, Liu F (2016) Strain engineering of graphene: a review. Nanoscale 8:3207–3217
[71] Zhang W-B, Qu Q, Zhu P, Lam C-H (2015) Robust intrinsic ferromagnetism and half semiconductivity in stable two-dimensional single-layer chromium trihalides. J Mater Chem C 3:12457–12468
[72] Kan M, Zhou J, Sun Q, Kawazoe Y, Jena P (2013) The intrinsic ferromagnetism in a $MnO_2$ monolayer. J Phys Chem Lett 4:3382–3386
[73] Du L, Hasan T, Castellanos-Gomez A, Liu G-B, Yao Y, Lau CN, Sun Z (2021) Engineering symmetry breaking in 2D layered materials. Nat Rev Phys 3:193–206
[74] Henkelman G, Uberuaga BP, Jonsson H (2000) A climbing image nudged elastic band method for finding saddle points and minimum energy paths. J Chem Phys 113:9901–9904
[75] Jiang P, Wang C, Chen D, Zhong Z, Yuan Z, Lu Z-Y, Ji W (2019) Stacking tunable interlayer magnetism in bilayer $CrI_3$. Phys Rev B 99:144401
[76] Sinn S, Kim CH, Kim BH, Lee KD, Won CJ, Oh JS, Han M, Chang YJ, Hur N, Sato H, Park B-G, Kim C, Kim H-D, Tae Won N (2016) Electronic structure of the Kitaev material α-$RuCl_3$ probed by photoemission and inverse photoemission spectroscopies. Sci Rep 6:39544
[77] Wang C, Zhou X, Pan Y, Qiao J, Kong X, Kaun C-C, Ji W (2018) Layer and doping tunable ferromagnetic order in two-dimensional $CrS_2$ layers. Phys Rev B 97:245409